# Unraveling dual phase transformations in a CrCoNi mediumentropy alloy

Yujie Chen<sup>1,2,3,&</sup>, Dengke Chen<sup>4,&</sup>, Xianghai An<sup>3,\*</sup>, Yin Zhang<sup>5</sup>, Zhifeng Zhou<sup>6</sup>, Song Lu<sup>7</sup>, Paul Munroe<sup>8</sup>, Sam Zhang<sup>1</sup>, Xiaozhou Liao<sup>3,\*</sup>, Ting Zhu<sup>5,\*</sup>, Zonghan Xie<sup>2</sup>

<sup>&</sup>lt;sup>1</sup>Centre for Advanced Thin Films and Devices, School of Materials and Energy, Southwest University, Chongqing 400715, China

<sup>&</sup>lt;sup>2</sup>School of Mechanical Engineering, The University of Adelaide, Adelaide, SA 5005, Australia

<sup>&</sup>lt;sup>3</sup>School of Aerospace, Mechanical and Mechatronic Engineering, The University of Sydney, Sydney, NSW 2006, Australia

<sup>&</sup>lt;sup>4</sup>State Key Laboratory of Ocean Engineering, Department of Engineering Mechanics, Shanghai Jiao Tong University, Shanghai, 200240, China

<sup>&</sup>lt;sup>5</sup>Woodruff School of Mechanical Engineering, Georgia Institute of Technology, Atlanta, GA 30332, USA

<sup>&</sup>lt;sup>6</sup>Hong Kong Branch of National Precious Metals Material Engineering Research Center (NPMM), City University of Hong Kong, Hong Kong, China

<sup>&</sup>lt;sup>7</sup>Applied Materials Physics, Department of Materials Science and Engineering, Royal Institute of Technology, Stockholm SE-100 44, Sweden

<sup>&</sup>lt;sup>8</sup>School of Materials Science and Engineering, The University of New South Wales, Sydney, NSW 2052, Australia

<sup>&</sup>amp;These authors contributed equally to this work

<sup>\*</sup>Corresponding authors: <u>xianghai.an@sydney.edu.au</u> (X.H. An); <u>xiaozhou.liao@sydney.edu.au</u> (X.Z. Liao); <u>ting.zhu@me.gatech.edu</u> (T. Zhu).

#### **Abstract**

The emergence of multi-principal element alloys (MPEAs) holds great promise for the development of high performance metallic materials. However, it remains unclear whether MPEAs can provide previously unknown deformation mechanisms to drastically enhance their mechanical performance. Here we report a new deformation mechanism of mechanically-induced dual phase transformations from the face-centered cubic (FCC) to hexagonal close-packed (HCP) phase and then back to the FCC phase with nanotwins in a CrCoNi medium-entropy alloy (MEA). During the two sequential steps of phase transformation, continued shear occurs in the same  $\langle 110\rangle_{FCC} \parallel \langle 11\bar{2}0\rangle_{HCP}$  direction along different  $\{111\}_{FCC} \parallel (0001)_{HCP}$  planes, producing a total shear transformation strain up to 70%. The dual phase transformations stem from a unique capability of facile slip in between the close-packed  $\{111\}_{FCC} \parallel \{0001\}_{HCP}$  atomic layers in both FCC and HCP phases, leading to flexible stacking sequences of those close-packed layers with low stacking fault energies. Our work demonstrates that MPEAs can offer unconventional deformation mechanisms such as dual phase transformations in the CrCoNi MEA, thereby opening opportunities for enhancing the mechanical properties of advanced alloys.

# **Keywords**

Medium-entropy alloy, phase transformation, deformation twinning, phase stability, stacking fault energy

#### 1. Introduction

Unlike traditional alloying strategies that are commonly based upon a single primary element, the novel design paradigm for high-entropy alloys (HEAs) and medium-entropy alloys (MEAs) incorporates multiple principal elements in equiatomic or near equiatomic concentrations that often form compositionally complex solid solutions [1-4]. This class of unconventional alloys has attracted considerable attention, since they open a new avenue of alloy design that has been little explored [5-13]. As the most-studied HEA, the Cantor alloy exhibits excellent mechanical properties at ambient and cryogenic temperatures [11, 12], due to progressive activation of various dislocation and/or twin-mediated deformation mechanisms [12-16]. As a prominent MEA, the CrCoNi alloy possesses an exceptional combination of strength, ductility and toughness, which surpasses that of most HEAs, MEAs and conventional alloys [10, 17]. The mechanistic aspects of plastic deformation in the CrCoNi alloy have been studied in terms of stress-induced twinning and phase transformation, which are largely related to its low or possibly negative stacking fault (SF) energy [7, 10, 17-21]. However, the deformation mechanisms reported for HEAs and MEAs so far have been observed in conventional metal alloys. It remains unclear whether a full exploration in a nearly infinite compositional space of multi-principal element alloys (MPEAs) can uncover previously unknown deformation mechanisms for enabling the drastically enhanced mechanical properties of metal alloys [22].

Although previous experiments showed that the face-centered-cubic (FCC) structure is predominant in CrCoNi-based HEAs and MEAs at room temperature [10-12, 21], theoretical investigations suggested that the hexagonal close-packed (HCP) structure is more stable due to its lower energy than FCC counterpart in these alloys [7]. These studies imply that the displacive phase transformation from the FCC to HCP structure in the CrCoNi alloy should be energetically favorable and therefore play an important role in governing its plastic responses and mechanical properties. In contrast to theoretical predictions [7], recent experimental

observations [21, 23] revealed the formation of massive deformation twins accompanied with a limited amount of the newly formed HCP phase (less than  $\sim$ 3% even when cryogenically deformed to a large strain of 53%) in CrCoNi. Based on the generalized SF energy curve (also called  $\gamma$ -surface), it was suggested that the FCC to HCP phase transformation may be kinetically limited due to the compositional complexity of multiple principal elements in CrCoNi [24, 25]. Incidentally, an intriguing observation is that the HCP laths formed are usually a few atomic layers thick and located next to FCC deformation twins [21], resulting in a composite structure of FCC-nanotwins and HCP-lamellae that cannot be readily interpreted on the basis of  $\gamma$ -surface. Therefore, it is imperative to understand the competitive and/or synergistic nature of these deformation mechanisms, in order to unravel the origin of superior mechanical properties of this alloy.

In this work, we use a combination of in situ micropillar compression testing, post mortem scanning transmission electron microscopy (STEM) imaging and atomistic simulation to uncover a previously unknown deformation mechanism of dual phase transformations in a nanostructured CrCoNi alloy that initially contains a mixture of FCC and HCP phases [26-28]. In particular, we perform atomic-scale characterization of several local regions from the outside to the center of the shear band in compressed micropillars. Since these regions experience increased shear strains, a spatial sequence of mapping uniquely reflects a time sequence of structural evolution and thereby provides direct evidence of sequential phase transformations from the FCC to HCP and back to FCC structure. Our combined experimental and modeling analyses further reveal the atomistic underpinning of sequential phase transformations in terms of facile slip between close-packed atomic layers in the CrCoNi alloy. These findings underscore the notion that MPEAs have the capacity of imparting new deformation mechanisms that can be harnessed for enhancing their mechanical performance.

## 2. Materials and methods

## 2.1. Material processing and sample preparation

A nanostructured CrCoNi film was deposited on an AISI M2 steel substrate (hardened to HRC 62, and polished to a final surface roughness of 0.01  $\mu$ m) using a DC magnetron sputtering system. The substrate was first cleaned by ultrasound before mounting on a stationary holder. The background chamber was pumped down to a pressure of  $4 \times 10^{-4}$  Pa prior to deposition. The argon gas (99.995% purity) was fed into the chamber at a constant flow rate of 50 sccm by an MKS mass flow controller and the chamber pressure was kept at 0.17 Pa during sputtering. A CrCoNi alloy target (Cr:Co:Ni = 1:1:1 at.%) with the purity of > 99.9% and dimensions of 345 × 145 × 5 mm³ was used for coating deposition. The target-to-substrate distance was set at 170 mm. Prior to deposition, the substrate was ion cleaned for 30 mins under a bias voltage of -450 V to remove all contaminants on the substrate surface. During the coating deposition, no external heating was used and a substrate bias voltage of -60 V was maintained. The CrCoNi target current (DC) was kept at 4.0 A and the sputtering power was  $\sim$ 1.5 kW, corresponding to a nominal deposition rate of  $\sim$ 72 nm/min, and the thickness of the CrCoNi film was about 5  $\mu$ m.

# 2.2. Structural characterization and in situ testing

Uniaxial compression specimens were fabricated using a dual-beam scanning electron microscope/focused ion beam (SEM/FIB) system (Helios Nanolab 600, FEI) from nanostructured CrCoNi films. We adopted three milling steps from a coarse milling condition of 30 kV and 0.28 nA to a fine milling condition of 30kV and 93 pA, and to a final superfine polishing condition of 30 kV and 9.7 pA, so as to minimize FIB damage. The FIB-milled pillars have diameters (D) of  $\sim$ 1  $\mu$ m and aspect ratios of height (H) to diameter of  $\sim$ 3. The tapering angle is  $\sim$ 1.5° and the diameters measured at approximately H/3 away from the pillar top were used to calculate engineering stresses [29]. Compression test was performed in an SEM using

a nanoindenter (PI 85 PicoIndenter, Hysitron Inc.) with a 5 μm diameter diamond flat punch. A displacement-control mode at a constant strain rate of 10<sup>-3</sup> s<sup>-1</sup> was applied during compression testing. The pillar was deformed to a prescribed displacement (or strain) followed by an incremental unloading. Transmission electron microscopy (TEM) samples of both asdeposited films and deformed pillars were prepared using the standard in situ lift-out technique [30] inside a dual beam SEM/FIB system (Helios Nanolab 600, FEI). The TEM lamellas were finally polished with a 5 kV and 24 pA Ga+ ion beam to minimize ion beam damage to the samples. Bright-field diffraction contrast imaging was performed using a Philips CM200 TEM operating at 200 kV. The high-angle annular dark-field (HAADF) STEM observations and energy-dispersive spectroscopy (EDS) compositional mapping were conducted using an aberration-corrected FEI Titan Themis TEM operating at 200 kV. SEM imaging of the compressed pillars was carried out at 10 kV in the same dual beam SEM/FIB.

#### 2.3. Atomistic simulation

Supplementary Figure 1 shows the atomic configurations of a CrCoNi alloy with the respective HCP, FCC and nanotwinned FCC structure. The simulation cell has the dimension of 6 nm × 13 nm × 7 nm and contains a total of ~50,000 atoms. Molecular statics simulations were performed with an embedded atom method (EAM) potential of CrCoNi [20] using LAMMPS [31]. Periodic boundary conditions were imposed in  $X - \langle 110 \rangle_{FCC}/\langle \bar{1}2\bar{1}0 \rangle_{HCP}$ ,  $Y - \langle 111 \rangle_{FCC}/[0001]_{HCP}$  and  $Z - \langle 112 \rangle_{FCC}/\langle 10\bar{1}0 \rangle_{HCP}$  directions. The shear strain  $\gamma_{yz}$  was applied to the simulation cell incrementally. The visualization tool OVITO [32] was employed to perform common neighbor analysis, so as to identify the FCC and HCP structures. For calculations of SF and cohesive energies, twenty random samples were used to obtain their mean values and standard deviations. At the annealing temperature of 800 K, the atomic structure was relaxed by rearrangement of Co, Cr, and Ni atoms using the Monte Carlo method [13, 20] in LAMMPS.

## 3. Results

## 3.1. Microstructure of as-deposited CrCoNi film

The as-deposited CrCoNi thin film exhibits a columnar nanograined structure with grain widths ranging from  $\sim 50$  to 150 nm (Figure 1a). The HAADF STEM image in Figure 1b and c show that within columnar nanograins, the HCP and FCC phases co-exist in a form of alternate nanolayers, which have the typical layer thickness of a few nanometers and the interphase orientation relationship of  $\{111\}_{FCC} \parallel (0001)_{HCP}$  and  $\langle 110\rangle_{FCC} \parallel \langle 11\bar{2}0\rangle_{HCP}$ . The  $\langle 111\rangle_{FCC} \parallel [0001]_{HCP}$  interface normal is oriented along the film growth direction. There is a strong grain texture along  $\langle 111\rangle_{FCC} \parallel [0001]_{HCP}$ , as evidenced by the selection area diffraction pattern (inset in Figure 1a). There are also many pre-existing planar defects including SFs and twin boundaries (TBs) in both phases (Figure 1c). Extensive STEM imaging confirmed that the alternate HCP and FCC layers, with the typical thicknesses of  $\sim 2$  to 10 nm, distributed through the columnar grains, and the volume fractions of HCP and FCC phases were statistically estimated based on the STEM images of 15 columnar grains to be  $\sim 60\%$  and  $\sim 40\%$ , respectively. The formation of such a highly-defective dual-phase structure in the CrCoNi thin film is attributed to the highly nonequilibrium processing condition of magnetron sputtering [26].

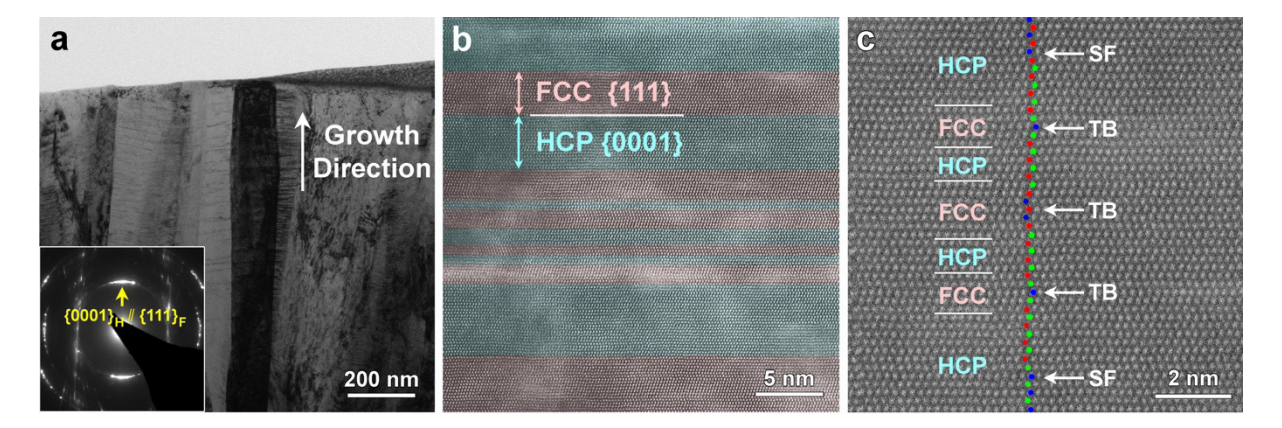


**Figure 1.** Microstructures of the as-deposited CrCoNi film. (a) Cross-sectional bright-field TEM image of the as-deposited CrCoNi film (with the corresponding electron diffraction pattern in the inset), showing the columnar grained nanostructure with grain widths ranging

from  $\sim 50$  to 150 nm and a strong  $\langle 111 \rangle_{FCC} \parallel [0001]_{HCP}$  texture along the film growth direction. (b) Typical HAADF STEM image of the atomic structure in the columnar grains, depicting the co-existence of the HCP and FCC phases, and the presence of a high density of planar defects, including SFs and TBs. (c) High resolution HAADF STEM image showing the coexisting HCP and FCC phases, containing SFs and TBs.

## 3.2. Dual phase transformations during deformation

Figure 2a presents the SEM image of a CrCoNi micropillar with an initial diameter of 1.02 µm, compressed to a strain of 7% when the first shear band formed. Supplementary Figure 2a shows the corresponding stress-strain curve. The HAADF STEM image in Figure 2b, which corresponds to the white-boxed region in Figure 2a, reveals the microstructure within and outside the shear band. Figure 2c shows the atomic structure of a region (enclosed by the red box in Figure 2b) right outside the shear band. This region underwent fairly large shear deformation and thus consisted of the HCP phase only, indicating the completion of the FCC to HCP phase transformation. The HCP phase in this region also contained multiple SFs. In contrast, Figure 2d shows the atomic structure of a region (enclosed by the yellow box in Figure 2b) inside the shear band. This region experienced much larger shear deformation than that in Figure 2c. More importantly, it consisted of a predominant FCC phase with nanotwins, accompanied by a small fraction of the HCP structure (Figure 2d). These observations provide direct evidence of the occurrence of a new deformation mechanism of dual phase transformations from the FCC to HCP and then nano-twinned FCC phase, thereby enabling extensive shear at the shear band. Supplementary Figure 3 lends further support to the operation of dual phase transformations by showing the atomic structure at different positions. Figure 2e presents the enlarged HAADF STEM image of an FCC/HCP interfacial region (corresponding to the green-boxed region in Figure 2d). It is seen that the FCC/HCP interface consists of Shockley partial dislocations with the Burgers vector of  $\frac{1}{6}\langle 112\rangle_{FCC} \parallel \frac{1}{3}\langle 1\bar{1}00\rangle_{HCP}$  (Figure 2e).

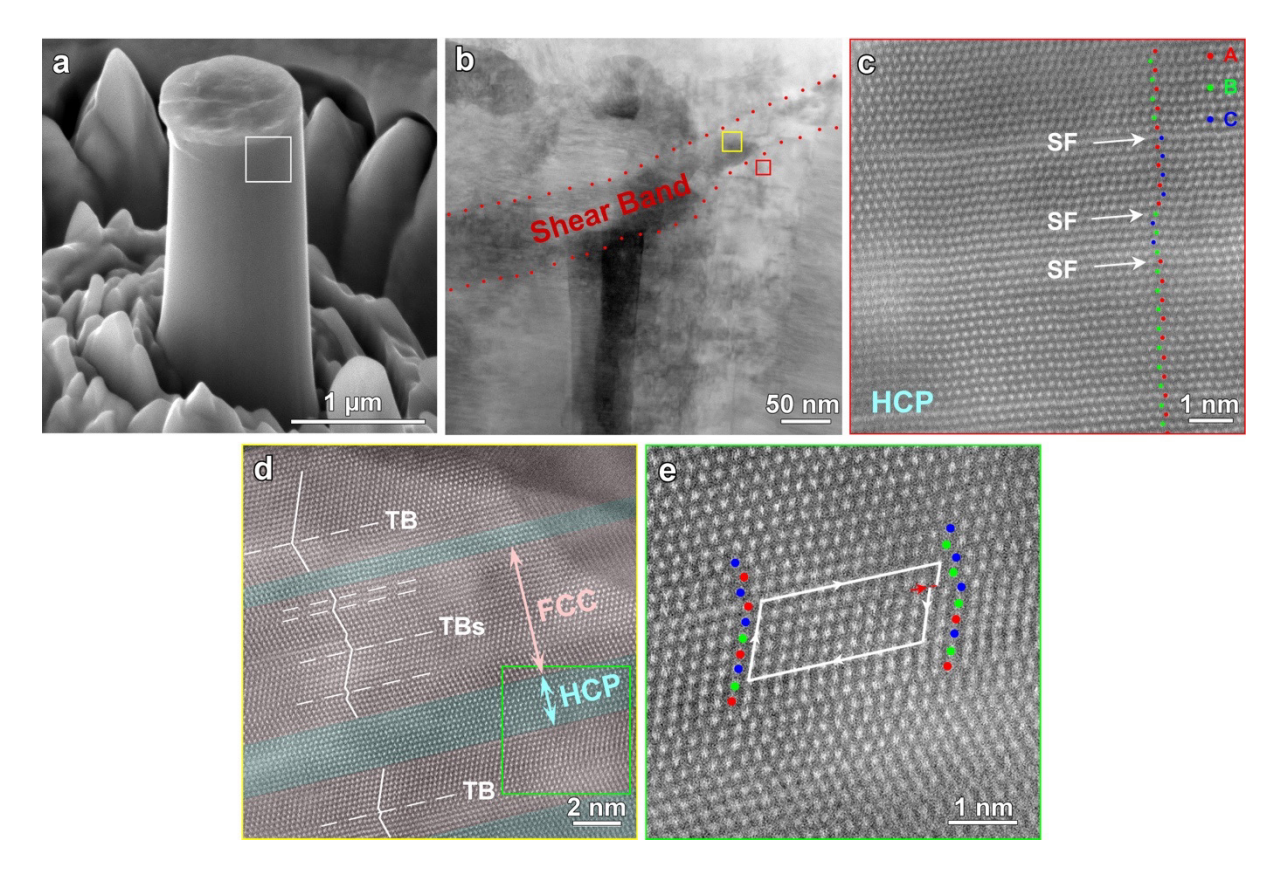


**Figure 2.** Dual phase transformations in a CrCoNi micropillar. (a) SEM image of a micropillar with diameter of 1.02 μm compressed to a strain of 7%. (b) STEM image of a shear band, corresponding to the boxed region in (a). (c) STEM image of the red-boxed region (just outside the shear band) in (b); this region exhibits a full HCP structure containing some SFs. The HCP structure is evidenced by the vertically marked atoms with a zigzag arrangement, showing the HCP stacking sequence of close-packed (0001)<sub>HCP</sub> atomic layers. (d) STEM image of the yellow-boxed region (inside the shear band) in (b); this region primarily consists of nanotwinned FCC structures with a small amount of HCP structures. (e) Magnified STEM image of the green-boxed region in (d), showing a Shockley partial dislocation identified through the Burgers loop analysis.

Dual phase transformations were often observed at the shear bands formed in compressed micropillars and usually accompanied with nanotwins. As another example of dual phase transformations, a large compressive strain up to 22% was applied to a micropillar (Figure 3) with an initial diameter of 0.94 µm similar to the one in Figure 2. The corresponding engineering stress–strain curve is shown in Supplementary Figure 2b. During in situ testing,

increased compression caused formation and thickening of an inclined shear band, which reached a thickness of about 40 nm at the compressive strain of 22% (Figures 3a and 3b). Since the local shear strain increased from the outside to the center of the shear band, we conducted a more detailed post mortem STEM characterization of the atomic structure in several regions located at different distances from the center of the shear band. These regions experienced different levels of shear strain and thus enabled the tracking of phase transformation sequences. They are enclosed by squares labeled as c, d, e, and f in Figure 3b, and the corresponding magnified STEM images are shown in Figures 3c, 3d, 3e, and 3f, respectively. Among those regions, region c is farthest from the center of the shear band and thus experienced the smallest shear strain. As seen from Figure 3c, region c consists of alternating HCP and FCC nanolayers (containing TBs and SFs), similar to the starting microstructure prior to compressive testing. In contrast, region d is closer to the shear band and thus experienced a larger shear strain than region c. The STEM image of region d (Figure 3d) shows the dominant HCP structure, mixed with a few nanotwinned FCC nanolayers. This microstructure indicates the occurrence of FCC → HCP transformation with increased shear. More interestingly, in regions even closer to the shear band such as region e (Figure 3e), the FCC structure containing FCC nanotwins became predominant, despite the presence of a small amount of the HCP structure. This result indicates that phase transformation took place from the HCP back to the FCC structure, leading to a further increase of lattice shear in the same direction. For region f (Figure 3f) inside the shear band, its atomic structure and fast Fourier transform (FFT) pattern (inset) reveal a single FCC phase containing FCC nanotwins with {111}<sub>FCC</sub> TBs. Therefore, the micropillar compression results in Figure 3 substantiate the occurrence of dual phase transformations through the sequential steps of FCC  $\rightarrow$  HCP  $\rightarrow$  FCC, thereby producing continuously increased lattice shear along the same direction.

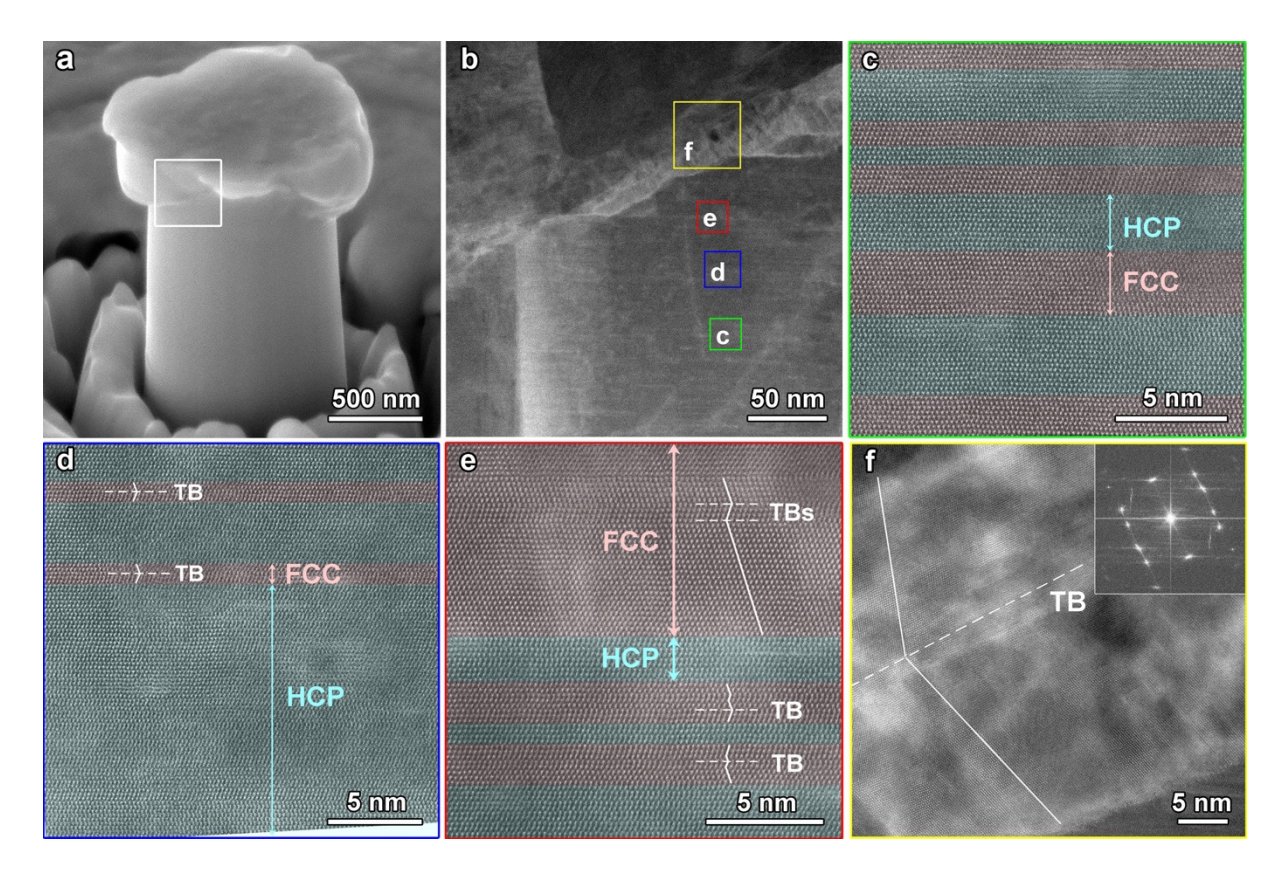


**Figure 3.** Structural evolution of the CrCoNi alloy at different locations near and within a major shear band. **(a)** SEM image of a micropillar compressed to a strain of 22%. **(b)** HAADF STEM image of the region enclosed by a white square in **(a)**, showing part of the shear band. **(c–f)** HAADF STEM images of regions **(c–f)** in **(b)**; these regions are marked by the green, blue, red, and yellow squares and experienced different levels of shear strain. **(c)** A region with small shear, exhibiting a mixture of FCC and HCP phases similar to the original microstructures. **(d)** A region with increased shear, showing the primary HCP structure with a small amount of nanotwinned FCC structures. **(e)** A region with larger shear than that in **(d)**, revealing the dominant FCC structure with nanotwins as well as a small amount of HCP structures. **(f)** Magnified STEM image of a severely sheared region (with the corresponding FFT pattern in the inset), showing a single FCC phase with a pair of nanotwin variants with a TB in the middle.

Apart from the phase transformations observed inside and next to the shear band, a similar mechanically-induced phase transformation pathway of FCC → HCP → nanotwinned FCC was also detected in other regions that experienced large deformation. As indicated in Fig. 4, almost fully nanotwinned FCC structures were observed in the area beneath the top surface

of the compressed micropillar (the boxed region in Figure 4a) that suffered severe shear deformation, and the HCP phase was rarely seen (Figure 4b–f). Incidentally, the energy-dispersive spectroscopy (EDS) mapping (Figure 5) shows uniform distributions of Cr, Co, and Ni in both as-deposited and deformed samples, which suggest a negligible effect of element distribution on dual phase transformations. Therefore, it is severe shear deformation that causes dual phase transformations in the CoCrNi MEA.

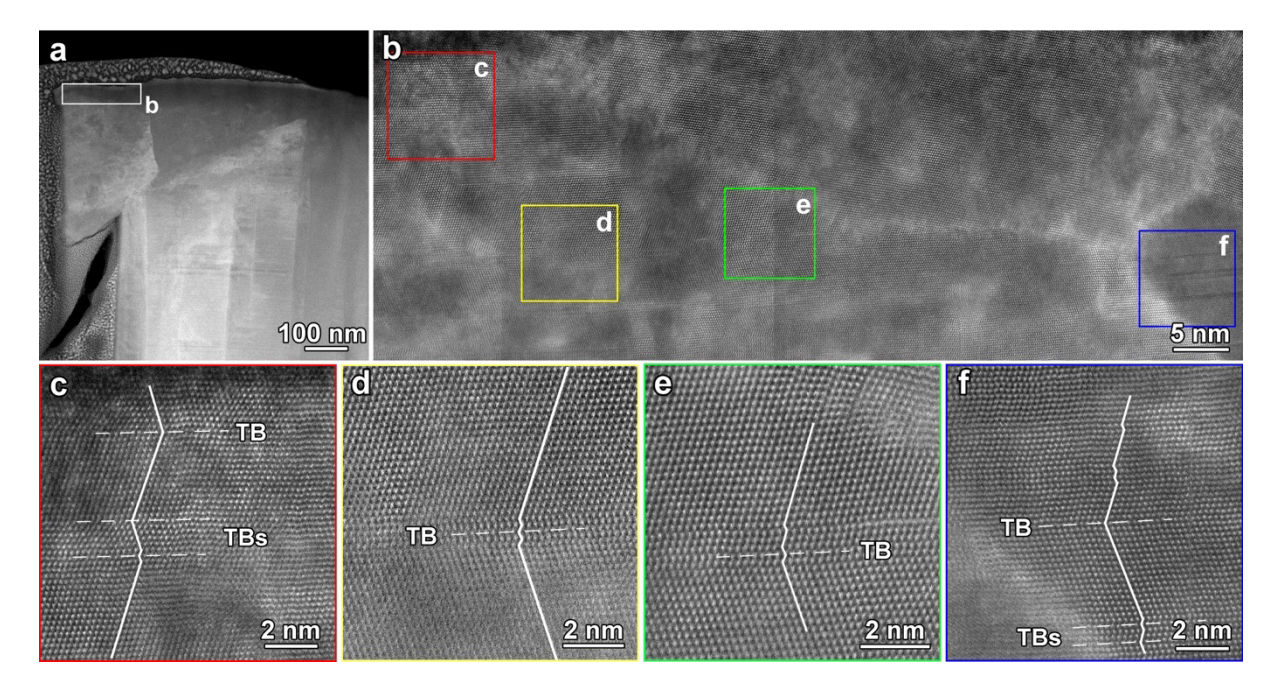


**Figure 4.** STEM images showing the FCC structure of the CrCoNi alloy in a highly deformed region. **(a)** STEM image of the pillar that has been compressed to a strain of 22%. **(b)** STEM image of the boxed region (beneath the top surface of the pillar) in **(a)**, showing a full FCC structure with twins and thus indicating the occurrence of HCP to twinned FCC phase transformation. **(c-f)** Magnified STEM images of the boxed regions in **(b)**, showing the common presence of FCC twins in a highly compressed pillar.

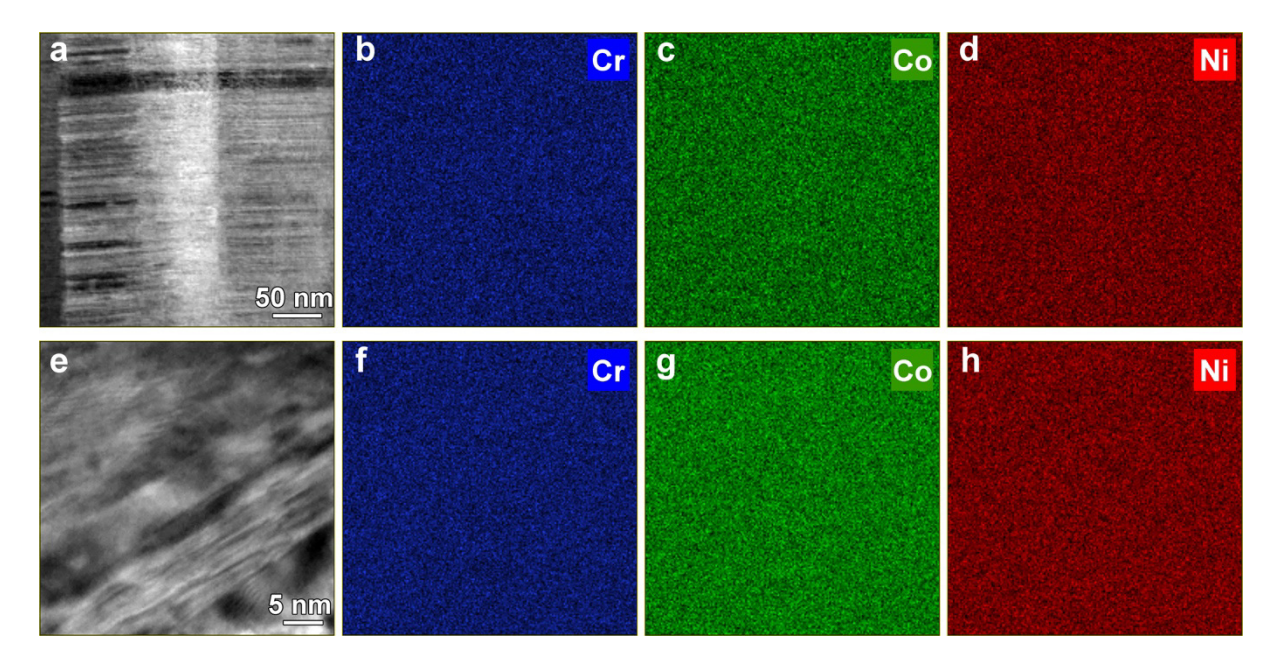


**Figure 5.** EDS mapping showing the uniform distribution of Cr, Co, and Ni in as-deposited and deformed samples. (a) STEM image of the EDS-mapped region including several dualphase (HCP and FCC) grains in an as-deposited sample. EDS element maps of the same region in (a) reveal the element distribution of (b) Cr, (c) Co, and (d) Ni. (e) STEM image of the EDS-mapped region of the shear band with FCC phase, from the pillar compressed to a strain of 22%. EDS element maps of the same region in (e) reveal the element distribution of (f) Cr, (g) Co, and (h) Ni.

#### 3.3. Atomistic mechanism

To illuminate the mechanistic origin of dual phase transformations, Figure 6 shows a schematic summary of the entire process of dual phase transformations accompanied with FCC nanotwinning. The initial microstructure consists of a mixture of alternating HCP and FCC nanolayers. It is common to observe SFs in both types of nanolayers as well as FCC nanotwins containing twin variants of FCC<sub>1</sub> (...ABCABC...) and FCC<sub>2</sub> (...CBACBA...). During the first step of dual phase transformations, FCC  $\rightarrow$  HCP occurs and the pre-existing HCP phase remains nearly unchanged, resulting in a nearly single HCP phase (Figures 2c and 6b). During the second step of dual phase transformations, HCP  $\rightarrow$  FCC occurs, yielding a complete FCC phase containing FCC nanotwins with thickness ranging from several to tens of nanometers.

The occurrence of such dual phase transformations of FCC  $\rightarrow$  HCP  $\rightarrow$  FCC may seem counterintuitive. Namely, if the phase transformation of FCC  $\rightarrow$  HCP was energetically favorable, the phase transformation of HCP  $\rightarrow$  FCC would be unfavored. Since the HCP  $\rightarrow$  FCC transformation was only observed near and inside shear bands, its occurrence must be a result of extensive shear at these shear bands (Figure 3f and 4b–f).

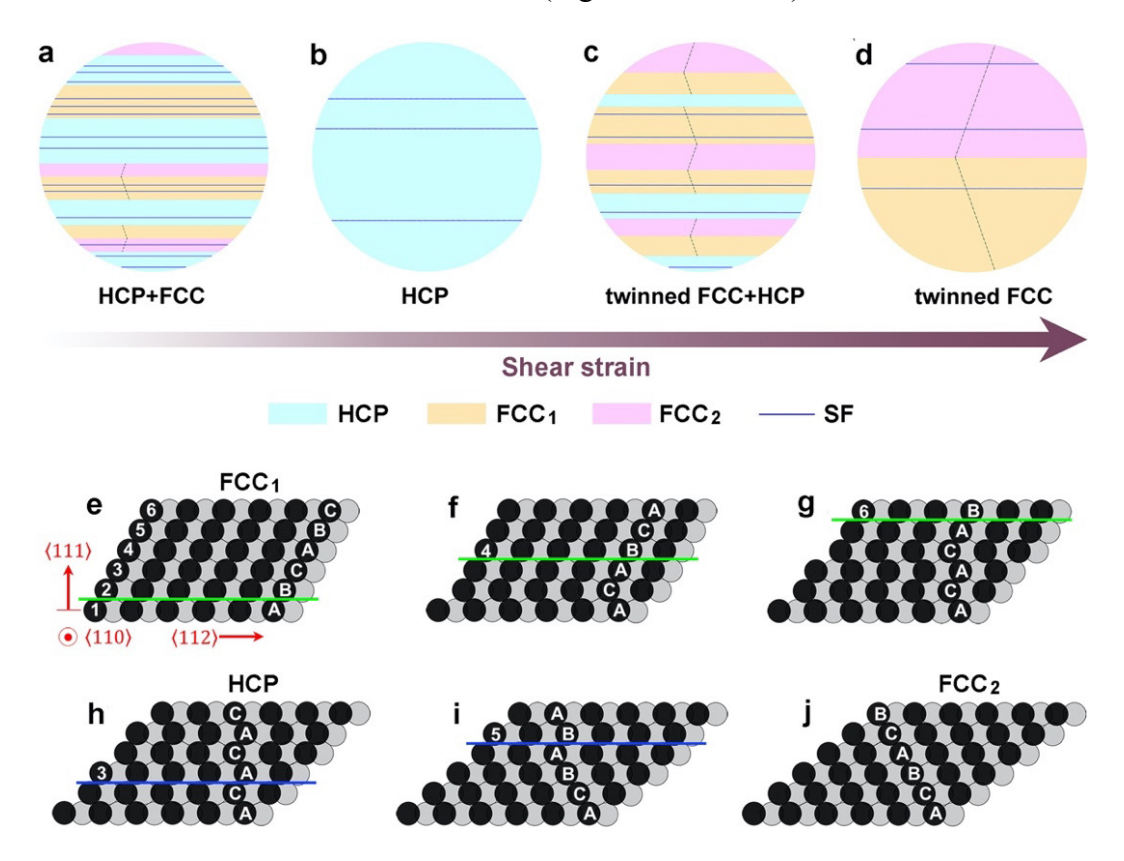


**Figure 6.** Schematic illustration of dual phase transformations and associated FCC nanotwinning in the CrCoNi alloy. (a) Coexisting HCP and FCC phases in an as-deposited sample. (b) Formation of an all HCP phase containing SFs during the initial stage of shear deformation. (c) Formation of a nanotwinned FCC structure in the HCP matrix due to continued shear in the same direction. (d) Further shear results in a complete transformation of the HCP to FCC phase, accompanied by FCC twin thickening. Here the light blue represents HCP; yellow FCC<sub>1</sub>; and pink FCC<sub>2</sub>; SFs are indicated by navy lines. (e-h) Atomistic pathways of transformation from the FCC<sub>1</sub> to HCP phase. The FCC<sub>1</sub> phase in (e) consists of the close-packed {111}<sub>FCC</sub> atomic layers with a stacking sequence of ...*ABCABC*...; these atomic layers are also labeled by 1, 2, 3..., so as to facilitate the tracking of their sequential slip. Atoms in alternate {110} planes are colored by gray and black, respectively. A sequence of slip (marked by green lines) occurs along the alternate close-packed planes as shown in (f) and (g). This

process results in the formation of the HCP structure, consisting of the close-packed {0001}<sub>HCP</sub> with a stacking sequence ...*ACACAC*..., as shown in **(h)**. **(h–j)** Atomistic pathways of transformation from the HCP to the FCC<sub>2</sub> phase through a sequence of slip (marked by blue lines) along a different set of alternate close-packed atomic planes. The newly formed FCC<sub>2</sub> phase and the initial FCC<sub>1</sub> phase exhibit a twin relationship.

Our combined experimental and modeling analyses indicate that the dual phase transformations stem from a unique capability of facile slip on the close-packed {111}<sub>FCC</sub> || (0001)<sub>HCP</sub> planes in both FCC and HCP phases of the CrCoNi alloy. As shown in Figure 6e– h, the FCC  $\rightarrow$  HCP transformation can be achieved readily by glide of Shockley partials with the Burgers vector  $\frac{1}{6}\langle 112\rangle_{FCC}$  on every other close-packed  $\{111\}_{FCC}$  plane. For example, the sequential slide of even-numbered layers 2, 4, 6 (as labeled in Figure 6e) can give rise to the FCC  $\rightarrow$  HCP phase transformation from an FCC<sub>1</sub> stacking sequence of ...ABCABC... to an HCP stacking sequence of ... ACACAC... (see Figure 6e-h). This transformation process produces a shear strain of 35%. More interestingly, the intermediate HCP phase can be transformed back to the FCC phase, giving a continued increase of shear strain in the same direction as the first step of FCC → HCP phase transformation. As shown in Figure 6h-j, the HCP → FCC transformation occurs by glide of Shockley partials with the same type of the Burgers vector of  $\frac{1}{3}\langle 1\bar{1}00\rangle_{HCP}$  as the FCC  $\rightarrow$  HCP transformation, but on a different set of close-packed (0001)<sub>HCP</sub> planes. That is, in the HCP phase with a stacking sequence of ... ACACAC..., the odd-numbered layers 3, 5 (as labelled in Figure 6e) slide sequentially (Figure 6h-i), resulting in the FCC<sub>2</sub> structure with a ...ABCABC... stacking sequence. This step of HCP  $\rightarrow$  FCC transformation also produces a shear strain of 35%, in the same shear direction as the first step of FCC  $\rightarrow$  HCP transformation. Consequently, the entire process of dual phase transformations produces a total shear transformation strain of 70%, thereby enabling extensive shear in those localized deformation bands. We note that the respective

shear transformation strains in the two sequential steps of phase transformation are identical and dictated purely by the lattice geometry of FCC and HCP structures, respectively, and thus independent of their lattice constants. The newly formed FCC<sub>2</sub> structure and the initial FCC<sub>1</sub> structure exhibit a twin relationship. Hence, nanotwins usually form when part of the FCC<sub>1</sub> structure is transformed to the FCC<sub>2</sub> structure. In as-deposited samples, both types of FCC variants, i.e., FCC<sub>1</sub> and FCC<sub>2</sub>, are present. When the respectively formed FCC<sub>2</sub> and FCC<sub>1</sub> variants meet in a largely sheared region, they merge to become a pair of thick twin variants with a TB in between (in Figure 6c and d). Such twin thickening results from the merging of thin twins or detwinning under mechanical loading [33-35].

The above analysis reveals atomistic pathways of dual phase transformations on the basis of a unique capability of facile slip between the close-packed  $\{111\}_{FCC} \parallel (0001)_{HCP}$ atomic layers in both FCC and HCP phases of the CrCoNi alloy. We next demonstrate that such facile slip is facilitated by low SF energies, leading to low energy cost associated with changes in stacking sequences of those close-packed atomic layers. Figure 7 shows the generalized SF energy curves along the pathway of formation of an SF in the FCC and HCP structure, respectively. This type of  $\gamma$ -surfaces was calculated using a recently developed EAM potential of the CrCoNi alloy that gives predictions close to first principles calculations [20]. In a perfect FCC structure, an increasing displacement of sliding in the  $\langle 112 \rangle_{FCC}$  direction was imposed along a {111}<sub>FCC</sub> plane, as indicated by the green line in Figure 6e. For each sliding increment, the system energy was minimized by the conjugate gradient method, while allowing interlayer relaxation perpendicular to the {111}<sub>FCC</sub> plane. This sliding process results in the formation of an SF with a local HCP stacking sequence of ... ACA... in the FCC structure as shown in Figure 6f. Figure 7a shows the corresponding  $\gamma$ -surface. The small negative SF value of -24 mJ/m<sup>2</sup> is consistent with previous first principles results in the literature [7]. This result demonstrates the accuracy of the EAM potential used in this work, and also suggests that the formation of local HCP packing in an FCC lattice can be energetically favorable in the CrCoNi alloy. The maximum on the  $\gamma$ -surface gives the unstable stacking energy of 305 mJ/m<sup>2</sup>, which represents the energy barrier of SF formation that needs to be overcome with the aid of applied shear stress and temperature.

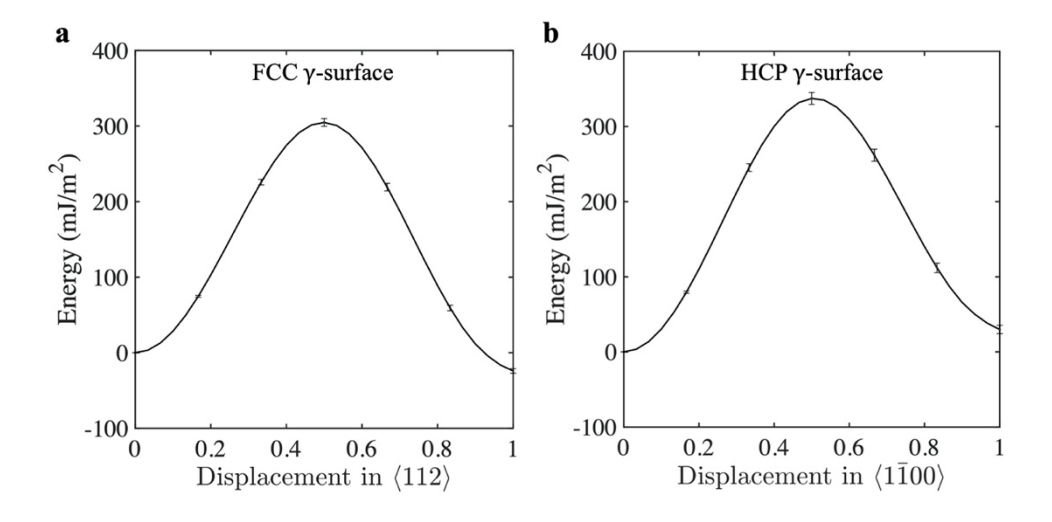
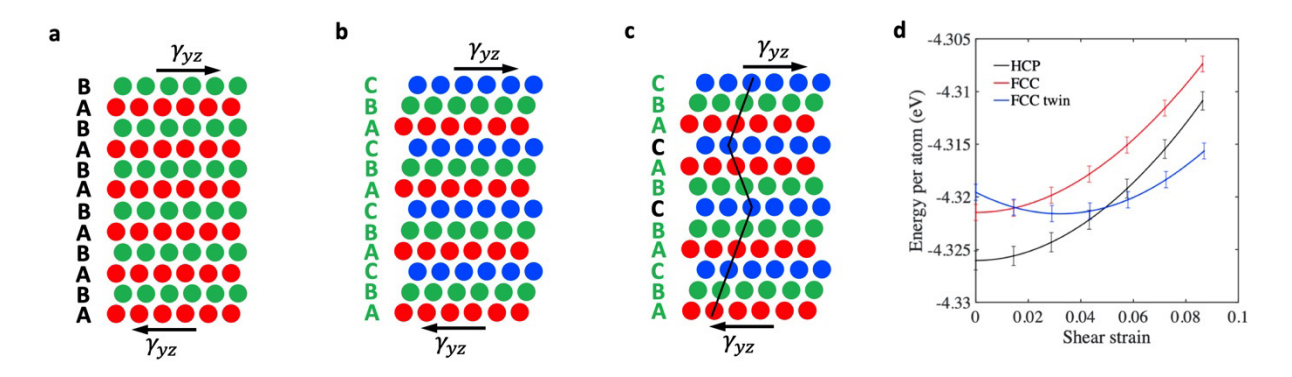


Figure 7. Generalized SF energy curves (i.e., γ-surface) of random CrCoNi alloys. (a) γ-surface for the shear displacement along  $\langle 112 \rangle_{FCC}$  across a  $\{111\}_{FCC}$  plane in the FCC structure. This shear displacement is normalized by  $1/6\langle 112 \rangle a_{FCC}$ , where  $a_{FCC} = 3.56 \text{Å}$  is the mean lattice constant. (b) γ-surface for the shear displacement along  $\langle 1\bar{1}00 \rangle_{HCP}$  across a  $(0001)_{HCP}$  plane in the HCP structure. This shear displacement is normalized by  $1/3\langle 1\bar{1}00 \rangle a_{HCP}$ , where  $a_{HCP} = 2.52 \text{Å}$  is the mean lattice constant. Mean energy values in (a) and (b) are respectively obtained by averaging the results from 20 samples with different random element distributions. Error bars correspond to the standard deviation.

Similar atomistic results were obtained for the energetics of SFs in the HCP phase. In an initially perfect HCP structure, an increasing displacement of sliding in the  $\langle 1\bar{1}00\rangle_{HCP}$  direction was imposed along a  $(0001)_{HCP}$  plane, as indicated by the blue line in Figure 6h. This sliding process in the HCP structure results in the formation of an SF with a local FCC stacking sequence of ...ABC..., as shown in Figure 6g. Figure 7b shows the corresponding  $\gamma$ -surface. The small positive SF energy of 30 mJ/m<sup>2</sup> is consistent with the similarly small SF energy in the FCC structure, despite opposite sign. It suggests low energy cost on the formation

of local FCC packing in an HCP lattice, which can become energetically favorable by a modest increase of applied shear stress. Moreover, the unstable stacking energy on the  $\gamma$ -surface in the HCP structure is 337 mJ/m², comparable to that in the FCC structure. This implies a similar level of energy barriers of SF formation in both HCP and FCC structures. In addition, as shown in Supplementary Figure 4, the  $\gamma$ -surfaces were calculated for both FCC and HCP structures with short-range ordering of alloy elements produced by simulated annealing for the CrCoNi alloy. These  $\gamma$ -surfaces give small positive SF energies in both structures. Hence, the similar  $\gamma$ -surfaces of the HCP and FCC structures with their characteristically low SF energies and close unstable stacking energies underlie the flexible stacking sequences of close-packed  $\{111\}_{FCC}$   $\parallel$   $(0001)_{HCP}$  atomic layers in the CrCoNi alloy. These  $\gamma$ -surface characteristics facilitate the dual phase transformations of FCC  $\rightarrow$  HCP  $\rightarrow$  FCC through facile slip across the close-packed  $\{111\}_{FCC}$   $\parallel$   $(0001)_{HCP}$  planes.



**Figure 8.** Schematic illustration showing the stacking sequences of (a) HCP structure, (b) FCC structure, and (c) FCC structure with a three-layer twin. (d) Cohesive energies (i.e., energy per atom) of the structures in (a-c) with increasing shear strain  $\gamma_{yz}$ . A lower value of cohesive energy at the same shear strain indicates that a more stable structure. The mean values and standard deviations were obtained by averaging twenty configurations with different random element distributions.

To understand the favorable formation of FCC nanotwins in the final FCC phase, we compared the cohesive energy per atom as a function of applied shear strain for the perfect HCP (Figure 8a), perfect FCC (Figure 8b), and nanotwinned FCC structure (Figure 8c). As shown in Figure 8d and Supplementary Figure 1, the HCP phase is energetically favorable at low shear strain (< ~ 5.5%). However, when the shear strain is above ~ 5.5%, the nanotwinned FCC structure has a lower lattice strain energy, despite an increase of TB energies. As a result, it possesses a lower cohesive energy than that of the strained HCP structure, while the strained FCC structure still has a larger cohesive energy than that of the strained HCP structure. This result lends support to the favorable formation of FCC nanotwins in the final FCC structure.

## 4. Discussion

A related phenomenon of bidirectional transformations between FCC and HCP phases was recently observed in the Fe<sub>50</sub>Mn<sub>30</sub>Co<sub>10</sub>Cr<sub>10</sub> HEA [36], and it was attributed to local dissipative heating and a near-zero yet positive SF energy value. Through this process, a hierarchical nanolaminate structure was developed with coexisting FCC and HCP phases. In contrast, our work on the CrCoNi alloy reveals the sequential phase transformations of FCC  $\rightarrow$  HCP  $\rightarrow$  FCC with increasing shear, resulting in a single-phase nanotwinned FCC structure. It remains unknown whether the Fe<sub>50</sub>Mn<sub>30</sub>Co<sub>10</sub>Cr<sub>10</sub> HEA could produce the sequential phase transformations of FCC  $\rightarrow$  HCP  $\rightarrow$  FCC, since its transformation sequence has not been clearly resolved and the local shear strain might not be sufficiently large in the work by Lu et al. [36]. Further comparative studies between the Fe<sub>50</sub>Mn<sub>30</sub>Co<sub>10</sub>Cr<sub>10</sub> HEA and the present CrCoNi MEA would enable a deeper understanding of dual phase transformations. In this regard, our results indicate that the sequential phase transformations of FCC  $\rightarrow$  HCP  $\rightarrow$  FCC stem from a unique capability of facile slip on the close-packed {111}<sub>FCC</sub> || (0001)<sub>HCP</sub> planes in both FCC and HCP phases of the CrCoNi alloy. The flexible stacking sequences of those close-packed atomic layers are facilitated by small SF energies in this alloy, as shown by our atomistic calculation

results (Figure 7) at zero K based on a recent EAM potential [20]. The small SF energies as well as the close FCC and HCP phase energies in the CrCoNi MEA should originate from the distribution and bonding of all three constituent elements in this alloy. Further studies are needed to understand the effects of electronic structure (e.g., magnetism [37]), short/medium-range atomic ordering and clustering [13, 38, 39], temperature [40, 41] on the energetics of SF formation and phase transformations in the CrCoNi alloy.

Dual phase transformations have not been revealed in previous studies of bulk CrCoNi MEAs [10, 17, 21, 23]. This may be due to a lack of atomistically detailed characterization of the structural evolution sequence in those studies or a lack of prevailing high stresses to overcome the energy barriers for dual phase transformations. In contrast, here we have examined several local regions from the outside to the center of a shear band, which experience increased shear strain. Such a spatial sequence of mapping uniquely reflects a time sequence of structural evolution and thus provides direct evidence of two sequential steps of FCC  $\rightarrow$ HCP → nanotwinned FCC transformation. The high stresses become more attainable in nanocrystalline CrCoNi alloys due to a generally established trend of "smaller being stronger". Such high stresses lower the energy barriers of dual phase transformations [42, 43]. In addition, the phase stability and phase transformation pathway can be affected by factors such as the initial grain texture [44, 45] as well as the initial FCC and HCP phase fractions [46, 47] in our nanostructured CrCoNi thin films, which contrast with the typical coarse-grained CrCoNi MEAs with a single FCC phase and random grain orientation. More specifically, the CrCoNi alloy sample in this study exhibits a strong  $\langle 111 \rangle_{FCC} \parallel [0001]_{HCP}$  grain texture along the film growth direction and also along the axial direction of the CrCoNi pillars (Fig. 1a and inset). Extensive high-resolution HAADF-STEM imaging (Figs. 1b and c) revealed that the HCP and FCC phases co-exist in a form of alternate nanolayers with an interphase orientation relationship of  $\{111\}_{FCC} \parallel (0001)_{HCP}$  and  $\langle 110\rangle_{FCC} \parallel \langle 11\bar{2}0\rangle_{HCP}$ . The  $\langle 111\rangle_{FCC} \parallel$ 

[0001] $_{\rm HCP}$  interface normal is oriented approximately along the film growth direction. The close-packed  $\{111\}_{\rm FCC} \parallel (0001)_{\rm HCP}$  atomic planes in FCC and HCP phases in the columnar grains are closely perpendicular to the loading direction. Hence, at low loads, there are low resolved shear stresses driving dislocation motion along those close-packed planes. With increasing load, localized shear banding occurred. Due to lattice rotation inside the shear band, large shear strains could be induced onto the rotated  $\{111\}_{\rm FCC} \parallel (0001)_{\rm HCP}$  planes, facilitating the movement of partial dislocations on the close-packed planes. This strain localization is critical to the occurrence of dual phase transformations. Future studies are needed to further understand the relative stability of FCC and HCP phases in the CrCoNi thin films and bulk CrCoNi alloys and clarify the effects of grain orientation on the phase transformation.

As shown in Fig. 1, the present CrCoNi MEA contains a mixture of alternating FCC and HCP phases. During the initial stage of shear deformation, FCC → HCP phase transformation competes with FCC deformation twinning through the conventional mode of layer-by-layer shear at TBs [48-50]. The former process can be favored by both the low and possibly negative SF energies in the FCC phase and the lower cohesive energies of the HCP relative to the FCC phase, as shown in Figure 7 and Figure 8. However, it is interesting to note that FCC deformation twinning can be effectively realized through a dual phase transformation pathway from the FCC to HCP and back to FCC phase (Figure 6). This unconventional FCC twinning mode also produces a total shear strain of 70%, same as the familiar mode of layer-by-layer twinning [48-50], but it offers an alternative to the conventional deformation twinning in producing extensive plastic shear. Moreover, the two sequential steps of phase transformation offer more facile means to relax local stresses and produce large plastic shear, thereby alleviating premature failure for improved ductility. For example, with the activation of dual phase transformations, local softening and hardening occur within the shear band and

they are manifested in the stress-strain curve of the CrCoNi pillars (Supplementary Figure 2b) [41, 51]. The hardening responses associated with the dual phase transformations could slow down the propagation of the shear bands and thus enhance the deformation resistance of the CrCoNi alloy.

#### 5. Conclusion

In summary, our experimental and modeling studies uncover a new deformation mechanism of mechanically-induced dual phase transformations from the FCC to HCP and then back to FCC phase, which produce continued shear up to 70% in the same direction in the CrCoNi MEA. The dual phase transformations stem from a unique capability of facile slip on the close-packed {111}<sub>FCC</sub> || (0001)<sub>HCP</sub> planes in both FCC and HCP phases of this MEA. Such dual phase transformations can produce intermediate HCP and FCC structures and their mixtures, enabling facile plastic deformation and high ductility of the CrCoNi alloy. The final formation of FCC twins is realized by dual phase transformations and thus distinctly different from the classical layer-by-layer twinning mechanism via gliding of twin partials on TBs in FCC crystals. These results will not only advance our knowledge about deformation physics and phase transformation of multi-component alloys, but also will motivate further exploration of dual phase transformations and other unconventional deformation mechanisms in MPEAs for enabling the drastically enhanced performance of metal alloys [52, 53].

# Acknowledgements

Z. H. Xie was supported by Australian Research Council (ARC) (DP200103152). X.H. An was supported by ARC (DE170100053) and the Robinson Fellowship Scheme of the University of Sydney (G200726). T. Zhu was supported by the U.S. National Science Foundation under grant number DMR-1810720. X.Z. Liao was supported by ARC (DP190102243). S. Zhang was

supported by Fundamental Research Funds for the Central Universities (SWU118105). The authors acknowledge the instruments and scientific and technical assistance of Microscopy Australia at the Adelaide Microscopy, The University of Adelaide. In particular, the authors would like to thank Dr. Animesh Basak and Dr. Ashley Slattery of Adelaide Microscopy for their support and expertise.

#### References

- [1] J.W. Yeh, S.K. Chen, S.J. Lin, J.Y. Gan, T.S. Chin, T.T. Shun, C.H. Tsau, S.Y. Chang, Nanostructured high-entropy alloys with multiple principal elements: novel alloy design concepts and outcomes, Adv. Eng. Mater. 6 (2004) 299-303.
- [2] E.P. George, D. Raabe, R.O. Ritchie, High-entropy alloys, Nat. Rev. Mater. 4 (2019) 515-534.
- [3] Y.F. Ye, Q. Wang, J.T. Lu, C.T. Liu, Y.C. Yang, High-entropy alloy: challenges and prospects, Mater. Today 19 (2016) 349-362.
- [4] D.B. Miracle, O.N. Senkov, A critical review of high entropy alloys and related concepts, Acta Mater. 122 (2017) 448-511.
- [5] H. Wang, D.K. Chen, X.H. An, Y. Zhang, S.J. Sun, Y.Z. Tian, Z.F. Zhang, A.G. Wang, J.Q. Liu, M. Song, S.P. Ringer, T. Zhu, X.Z. Liao, Deformation-induced crystalline-to-amorphous phase transformation in a CrMnFeCoNi high-entropy alloy, Sci. Adv. 7 (2021) eabe3105.
- [6] Q.Q. Ding, X.Q. Fu, D.K. Chen, H.B. Bei, B. Gludovatz, J.X. Li, Z. Zhang, E.P. George, Q. Yu, T. Zhu, Real-time nanoscale observation of deformation mechanisms in CrCoNi-based medium-to high-entropy alloys at cryogenic temperatures, Mater. Today 25 (2019) 21-27.

- [7] Z.J. Zhang, H.W. Sheng, Z.J. Wang, B. Gludovatz, Z. Zhang, E.P. George, Q. Yu, S.X. Mao, R.O. Ritchie, Dislocation mechanisms and 3D twin architectures generate exceptional strength-ductility-toughness combination in CrCoNi medium-entropy alloy, Nat. Commun. 8 (2017) 14390.
- [8] Z.F. Lei, X.J. Liu, Y. Wu, H. Wang, S.H. Jiang, S.D. Wang, X.D. Hui, Y.D. Wu, B. Gault, P. Kontis, D. Raabe, L. Gu, Q.H. Zhang, H.W. Chen, H.T. Wang, J.B. Liu, K. An, Q.S. Zeng, T.G. Nieh, Z.P. Lu, Enhanced strength and ductility in a high-entropy alloy via ordered oxygen complexes, Nature 563 (2018) 546.
- [9] C. Varvenne, A. Luque, W.A. Curtin, Theory of strengthening in fcc high entropy alloys, Acta Mater. 118 (2016) 164-176.
- [10] B. Gludovatz, A. Hohenwarter, K.V. Thurston, H.B. Bei, Z.G. Wu, E.P. George, R.O. Ritchie, Exceptional damage-tolerance of a medium-entropy alloy CrCoNi at cryogenic temperatures, Nat. Commun. 7 (2016) 10602.
- [11] B. Gludovatz, A. Hohenwarter, D. Catoor, E.H. Chang, E.P. George, R.O. Ritchie, A fracture-resistant high-entropy alloy for cryogenic applications, Science 345 (2014) 1153-1158.
- [12] S.J. Sun, Y.Z. Tian, X.H. An, H.R. Lin, J.W. Wang, Z.F. Zhang, Ultrahigh cryogenic strength and exceptional ductility in ultrafine-grained CoCrFeMnNi high-entropy alloy with fully recrystallized structure, Mater. Today Nano 4 (2018) 46-53.
- [13] Q.Q. Ding, Y. Zhang, X. Chen, X.Q. Fu, D.K. Chen, S.J. Chen, L. Gu, F. Wei, H.B. Bei, Y.F. Gao, M.R. Wen, J.X. Li, Z. Zhang, T. Zhu, R.O. Ritchie, Q. Yu, Tuning element distribution, structure and properties by composition in high-entropy alloys, Nature 574 (2019) 223-227.
- [14] Z.J. Zhang, M.M. Mao, J.W. Wang, B. Gludovatz, Z. Zhang, S.X. Mao, E.P. George, Q. Yu, R.O. Ritchie, Nanoscale origins of the damage tolerance of the high-entropy alloy CrMnFeCoNi, Nat. Commun. 6 (2015) 10143.

- [15] F. Otto, A. Dlouhý, C. Somsen, H.B. Bei, G. Eggeler, E.P. George, The influences of temperature and microstructure on the tensile properties of a CoCrFeMnNi high-entropy alloy, Acta Mater. 61 (2013) 5743-5755.
- [16] Q.Y. Lin, X.H. An, H.W. Liu, Q.H. Tang, P.Q. Dai, X.Z. Liao, In-situ high-resolution transmission electron microscopy investigation of grain boundary dislocation activities in a nanocrystalline CrMnFeCoNi high-entropy alloy, J. Alloys Compd. 709 (2017) 802-807.
- [17] G. Laplanche, A. Kostka, C. Reinhart, J. Hunfeld, G. Eggeler, E.P. George, Reasons for the superior mechanical properties of medium-entropy CrCoNi compared to high-entropy CrMnFeCoNi, Acta Mater. 128 (2017) 292-303.
- [18] S. Huang, H. Huang, W. Li, D. Kim, S. Lu, X.Q. Li, E. Holmström, S.K. Kwon, L. Vitos, Twinning in metastable high-entropy alloys, Nat. Commun. 9 (2018) 2381.
- [19] J. Ding, Q. Yu, M. Asta, R.O. Ritchie, Tunable stacking fault energies by tailoring local chemical order in CrCoNi medium-entropy alloys, Proc. Natl. Acad. Sci. U.S.A. 115 (2018) 8919-8924.
- [20] Q.-J. Li, H. Sheng, E. Ma, Strengthening in multi-principal element alloys with local-chemical-order roughened dislocation pathways, Nat. Commun. 10 (2019) 3563.
- [21] J.S. Miao, C.E. Slone, T.M. Smith, C. Niu, H.B. Bei, M. Ghazisaeidi, G.M. Pharr, M.J. Mills, The evolution of the deformation substructure in a Ni-Co-Cr equiatomic solid solution alloy, Acta Mater. 132 (2017) 35-48.
- [22] E.P. George, W. Curtin, C.C. Tasan, High entropy alloys: A focused review of mechanical properties and deformation mechanisms, Acta Mater. 188 (2020) 435-474.
- [23] F.X. Zhang, S.J. Zhao, K. Jin, H.B. Bei, D. Popov, C. Park, J.C. Neuefeind, W.J. Weber, Y.W. Zhang, Pressure-induced fcc to hcp phase transition in Ni-based high entropy solid solution alloys, Appl. Phys. Lett. 110 (2017) 011902.

- [24] M.B. Kivy, M.A. Zaeem, Generalized stacking fault energies, ductilities, and twinnabilities of CoCrFeNi-based face-centered cubic high entropy alloys, Scr. Mater. 139 (2017) 83-86.
- [25] Q.Y. Lin, J.P. Liu, X.H. An, H. Wang, Y. Zhang, X.Z. Liao, Cryogenic-deformation-induced phase transformation in an FeCoCrNi high-entropy alloy, Mater. Res. Lett. 6 (2018) 236-243.
- [26] Y.J. Chen, Z.F. Zhou, P. Munroe, Z.H. Xie, Hierarchical nanostructure of CrCoNi film underlying its remarkable mechanical strength, Appl. Phys. Lett. 113 (2018) 081905.
- [27] S.J. Tsianikas, Y.J. Chen, Z.H. Xie, Deciphering deformation mechanisms of hierarchical dual-phase CrCoNi coatings, J. Mater. Sci. Technol. 39 (2020) 7-13.
- [28] Y.J. Chen, X.H. An, Z.F. Zhou, P. Munroe, S. Zhang, X.Z. Liao, Z.H. Xie, Size-dependent deformation behavior of dual-phase, nanostructured CrCoNi medium-entropy alloy, Sci. China Mater. 64 (2021) 209-222.
- [29] J.R. Greer, W.D. Nix, Nanoscale gold pillars strengthened through dislocation starvation, Phys. Rev. B 73 (2006) 245410.
- [30] L.A. Giannuzzi, F.A. Stevie, A review of focused ion beam milling techniques for TEM specimen preparation, Micron 30 (1999) 197-204.
- [31] S. Plimpton, Fast parallel algorithms for short-range molecular dynamics, J. Comput. Phys. 117 (1995) 1-19.
- [32] A. Stukowski, Visualization and analysis of atomistic simulation data with OVITO-the Open Visualization Tool, Model. Simul. Mat. Sci. Eng. 18 (2009) 015012.
- [33] S.C. Zhao, Q. Zhu, X.H. An, H. Wei, K.X. Song, S.X. Mao, J.W. Wang, In situ atomistic observation of the deformation mechanism of Au nanowires with twin–twin intersection, J. Mater. Sci. Technol. 53 (2020) 118-125.

- [34] J. Wang, N. Li, O. Anderoglu, X.H. Zhang, A. Misra, J.Y. Huang, J.P. Hirth, Detwinning mechanisms for growth twins in face-centered cubic metals, Acta Mater. 58 (2010) 2262-2270. [35] Y. Cao, Y.B. Wang, X.H. An, X.Z. Liao, M. Kawasaki, S.P. Ringer, T.G. Langdon, Y.T. Zhu, Grain boundary formation by remnant dislocations from the de-twinning of thin nanotwins, Scr. Mater. 100 (2015) 98-101.
- [36] W.J. Lu, C.H. Liebscher, G. Dehm, D. Raabe, Z.M. Li, Bidirectional Transformation Enables Hierarchical Nanolaminate Dual-Phase High-Entropy Alloys, Adv. Mater. 30 (2018) 1804727.
- [37] C.N. Niu, C.R. LaRosa, J.S. Miao, M.J. Mills, M. Ghazisaeidi, Magnetically-driven phase transformation strengthening in high entropy alloys, Nat. Commun. 9 (2018) 1363.
- [38] F.-H. Cao, Y.-J. Wang, L.-H. Dai, Novel atomic-scale mechanism of incipient plasticity in a chemically complex CrCoNi medium-entropy alloy associated with inhomogeneity in local chemical environment, Acta Mater. 194 (2020) 283-294.
- [39] F. Walsh, M. Asta, R.O. Ritchie, Magnetically driven short-range order can explain anomalous measurements in CrCoNi, Proc. Natl. Acad. Sci. U.S.A. 118 (2021) e2020540118.
- [40] S. Huang, W. Li, E. Holmström, S.K. Kwon, O. Eriksson, L. Vitos, Plastic deformation transition in FeCrCoNiAl x high-entropy alloys, Mater. Res. Lett. 7 (2019) 439-445.
- [41] J.P. Liu, X.X. Guo, Q.Y. Lin, Z.B. He, X.H. An, L.F. Li, P.K. Liaw, X.Z. Liao, L.P. Yu, J.P. Lin, Excellent ductility and serration feature of metastable CoCrFeNi high-entropy alloy at extremely low temperatures, Sci. China Mater. 62 (2019) 853-863.
- [42] J.Y. Huang, Y.K. Wu, H.Q. Ye, Allotropic transformation of cobalt induced by ball milling, Acta Mater. 44 (1996) 1201-1209.
- [43] J. Su, X. Wu, D. Raabe, Z. Li, Deformation-driven bidirectional transformation promotes bulk nanostructure formation in a metastable interstitial high entropy alloy, Acta Mater. 167 (2019) 23-39.

- [44] Z.S. You, X.Y. Li, L.J. Gui, Q.H. Lu, T. Zhu, H.J. Gao, L. Lu, Plastic anisotropy and associated deformation mechanisms in nanotwinned metals, Acta Mater. 61 (2013) 217-227.
- [45] T. Zhu, H.J. Gao, Plastic deformation mechanism in nanotwinned metals: an insight from molecular dynamics and mechanistic modeling, Scr. Mater. 66 (2012) 843-848.
- [46] Z.M. Li, C.C. Tasan, K.G. Pradeep, D. Raabe, A TRIP-assisted dual-phase high-entropy alloy: grain size and phase fraction effects on deformation behavior, Acta Mater. 131 (2017) 323-335.
- [47] Q. Fang, Y. Chen, J. Li, C. Jiang, B. Liu, Y. Liu, P.K. Liaw, Probing the phase transformation and dislocation evolution in dual-phase high-entropy alloys, Int. J. Plast. 114 (2019) 161-173.
- [48] Y.T. Zhu, X.Z. Liao, X.L. Wu, Deformation twinning in nanocrystalline materials, Prog. Mater. Sci. 57 (2012) 1-62.
- [49] J.W. Christian, S. Mahajan, Deformation twinning, Prog. Mater. Sci. 39 (1995) 1-157.
- [50] X.H. An, S.D. Wu, Z.G. Wang, Z.F. Zhang, Significance of stacking fault energy in bulk nanostructured materials: Insights from Cu and its binary alloys as model systems, Prog. Mater. Sci. 101 (2019) 1-45.
- [51] Z. Cai, H. Ding, R. Misra, Z. Ying, Austenite stability and deformation behavior in a cold-rolled transformation-induced plasticity steel with medium manganese content, Acta Mater. 84 (2015) 229-236.
- [52] D. Raabe, Z.M. Li, D. Ponge, Metastability alloy design, MRS Bulletin 44 (2019) 266-272.
- [53] E. Ma, X.L. Wu, Tailoring heterogeneities in high-entropy alloys to promote strength–ductility synergy, Nat. Commun. 10 (2019) 5623.